Electrospun Bismuth Ferrite Nanofibers for Potential Applications in Ferroelectric Photovoltaic Devices

Linfeng Fei,[⊥,‡] Yongming Hu,[*,⊥,§] Xing Li,[‡] Ruobing Song,[‡] Li Sun,[‡] Haitao Huang,[‡] Haoshuang Gu,[§] Helen L. W. Chan,[‡] and Yu Wang[*,‡]

[‡]Department of Applied Physics and Materials Research Center, The Hong Kong Polytechnic University, Hong Kong SAR, China

[§]Key Laboratory of Ferro- & Piezoelectric Materials and Device of Hubei Province, Faculty of Physics and Electronic Science, Hubei University, Wuhan, China

S *Supporting Information*

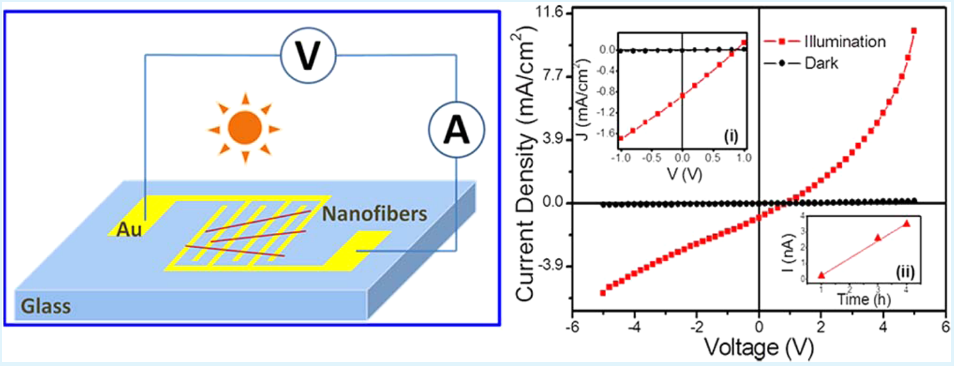

ABSTRACT: Bismuth ferrite (BFO) nanofibers were synthesized via a sol–gel-based electrospinning process followed by thermal treatment. The influences of processing conditions on the final structure of the samples were investigated. Nanofibers prepared under optimized conditions were found to have a perovskite structure with good quality of crystallization and free of impurity phase. Ferroelectric and piezoelectric responses were obtained from individual nanofiber measured on a piezoelectric force microscope. A prototype photovoltaic device using laterally aligned BFO nanofibers and interdigital electrodes was developed and its performance was examined on a standard photovoltaic system. The BFO nanofibers were found to exhibit an excellent ferroelectric photovoltaic property with the photocurrent several times larger than the literature data obtained on BFO thin films.

KEYWORDS: *bismuth ferrite, nanofibers, electrospinning, heat treatment, piezoelectric force microscope, photovoltaic, interdigital electrode*

■ INTRODUCTION

Bismuth ferrite ($BiFeO_3$; abbreviated as BFO) is a metallic oxide with a simple composition but rich physical and chemical properties. It has a rhombohedraly distorted perovskite structure (space group *R*3*c*) and is the only multiferroic compound which exhibits coupled ferroelectric and antiferromagnetic orders (i.e., the magnetoelectric effect) well above room temperature.[1−3] The intrinsic magnetoelectric effect in bulk BFO is very weak but could be significantly enhanced in thin films through lattice engineering—an effect that can also be observed in thin films of many other functional oxides.[3−8] This discovery[3] and the expectation of utilizing BFO thin films for new information storage devices have stimulated worldwide research interest over the last 10 years, which led to the discovery of many other interesting physical/chemical properties (gas sensing, visible light photocatalytic behaviors, etc.) in nanostructures of this material system.[9−13] More recently, it was reported that BFO can produce significant switchable photocurrent and photovoltage under the illumination of visible light; i.e., the so-called ferroelectric photovoltaic effect.[14−19] Compared with typical semiconducting photovoltaic materials, BFO has a rather low photovoltaic coefficient and is thus far from practical applications. Moreover, a clear physical picture about the photovoltaic mechanism is not yet available despite several models having been proposed in the literature. Therefore, there is currently increasing interest to study both the fundamental and applied aspect of the ferroelectric photovoltaic behaviors of BFO.

In the literature, BFO-based photovoltaic devices have a common parallel-capacitor type of structure (also referred as a metal—insulator—metal "sandwich" structure). The advantage for such structure is that devices can be made using standard semiconducting technology using a buffer layer (despite there is actually a technical compatibility issue due to the volatility of

Received: November 19, 2014
Accepted: January 26, 2015
Published: January 26, 2015

DOI: 10.1021/acsami.5b00069
ACS Appl. Mater. Interfaces 2015, 7, 3665−3670

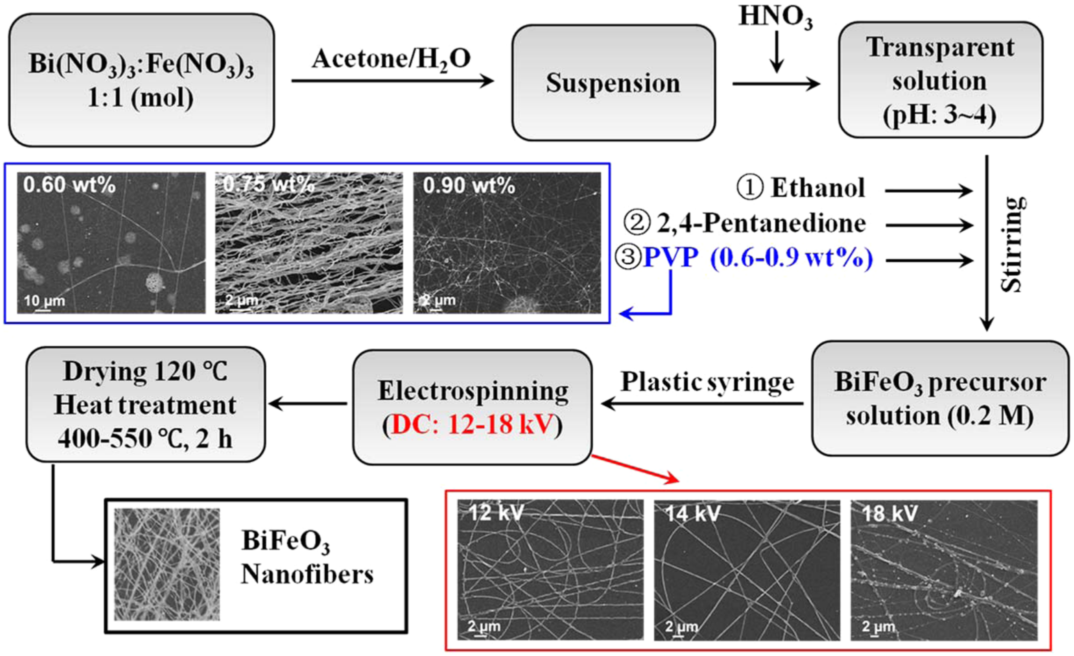

Figure 1. Flowchart of the precursor preparation and nanofiber synthesis. Insets: (blue) morphology of nanofibers prepared using different amount of PVP in solutions −0.6, 0.75, and 0.9 wt %.; and (red) morphology of nanofibers synthesized at different accelerating voltages −12, 14, and 18 kV.

bismuth at high temperature).[20−22] The problems associated with such configuration are that the devices may exhibit (1) low output voltages because the output voltage of a single "sandwich" is proportional to film thickness (typically <1 μm) and (2) suppressed ferroelectric polarization due to the clamping effect from the substrate and hence relatively poor photovoltaic coefficient. In light of this situation, we propose to develop BFO-nanofiber based photovoltaic devices with a new configuration of nanofibers/IDE/substrate (where IDE refers to "interdigital electrode"). In our structure, much higher output voltage could be obtained because it is now proportional to the length of BFO nanofibers (which could be > several micrometers long). Meanwhile, the nanofibers are free-standing and free of substrate clamping effect. It is noted that such laterally aligned structures have been adopted in energy-harvesting systems such as piezoelectric nanogenerators but not yet used in photovoltaic devices.[22]

To make devices with the above-mentioned configuration, the development of high-quality BFO nanofibers is a critical step. In this work, the electrospinning method was employed as it is a feasible and scalable technique for making nanofibers by utilizing an electrical charge to draw fibers from a liquid with suitable viscosity.[23,24] Because of thermodynamic reasons, the synthesis of bulk BFO via solid-state reaction is often associated with the formation of impurity phases (such as Bi_2O_3/$Bi_2Fe_4O_9$), which could be effectively suppressed via rapid annealing.[25,26] A similar problem would occur in the synthesis of BFO nanostructures through chemical routes unless processing parameters are carefully optimized. Among the chemical processes in the literature, a soft chemical method first reported by Ghosh et al. is relatively easy to handle as it simply involves the use of tartaric acid as a template material and nitric acid as an oxidizing agent, meanwhile the crystallization of BFO could be realized at relatively low temperature and under ambient pressure.[27,28] As to be demonstrated in this paper, we managed to modify the soft chemical method through which high-quality nanofibers of BFO were obtained. The electrical measurements indicate that the nanofibers are ferroelectric and exhibit excellent photovoltaic performance.

■ EXPERIMENTAL SECTION

Precursor Solution Preparation. The precursors were prepared via a sol−gel process. All start chemicals were of analytical grade. In a typical procedure, 1.20 g of bismuth nitrate ($Bi(NO_3)_3{\cdot}SH_2O$) and 1.00 g of iron nitrate ($Fe(NO_3)_3{\cdot}9H_2O$) were weighed and dissolved into a mixture of 10 mL of acetone and 5 mL of distilled water, followed by exposure to ultrasound for 5 min to give a suspended solution. Then 1 mL of nitric acid (67%, mass ratio) was added dropwise until the suspended solution became transparent. After that, a 7.5 g solution of 10% (mass concentration) poly(vinylpyrrolidone) (PVP, molecular weight of about 1 300 000) in ethanol was added dropwise and stirred for 30 min. Finally, 1 mL of 2, 4-pentanedione (99^+ %) was added dropwise to the solution to form the precursor solution.

Electrospinning. The processing conditions were (i) capillary-collector distance = 10 cm, (ii) accelerating voltage = 14 kV, and (iii) solution feeding rate = 0.5 mL/h. The as-spun fibers (collected on Al foil, Au/glass wafer, or Au/SiO_2/Si wafer) were then dried at 120 °C for 2 h. Thermogravimetric analysis and differential scanning calorimetry were conducted on a TG-DSC system (NETZSCH STA 449 C Jupiter). On the basis of the analytical results, the thermal annealing were conducted at temperatures from 400 to 600 °C for 2 h in ambient conditions.

Structural Characterizations. Annealed samples were characterized using X-ray diffraction (XRD) with a Bruker AXS D8 ADVANCE X-ray diffractometer with Cu Kα radiation (λ = 0.154178 nm). Scanning electron microscopy (SEM) observations were carried out on a JEOL 6335F system. Transmission electron microscopy (TEM) images and EDS spectra were obtained on JEOL 2011 and 2100F (field-emission) transmission electron microscopes at an acceleration voltage of 200 kV. And the topography and the piezoresponse tests were taken on a Veeco Multimode SPM system with Nanoscope IV controller.

Electrical and Photovoltaic Characterizations. The optical responses of BFO nanofibers were examined using a symmetric electrode to eliminate the effects of different work function of the electrodes and asymmetric Schottky−Ohmic contacts on the photovoltaic properties (asymmetric Schottky−Ohmic contact can also produce diode-like photocurrent). Au IDEs were sputtered on highly transparent glass substrate. The nanofibers were deposited on Au IDE by electrospinning. Before optical measurement, the BFO nanofibers were poled under a voltage of 200 V, much larger than external bias applied during measurement (5 V). The photocurrent−-photovoltage response was measured under AM 1.5G illumination (100 mW/cm^2) provided by a solar simulator (model 91160, Newport-Oriel Instruments, USA) with an AM 1.5 filter, and the photocurrent was recorded by an electrometer (Keithley 6517b).

RESULTS AND DISCUSSION

1. Processing Optimization and Structures of Nanofibers. The precursor solution for electrospinning was prepared via a soft chemical method, as shown in the flowchart in Figure 1. Different from conventional soft chemical route for the synthesis of nanoparticles, the solutions we used in this work contained a large portion of poly(vinylpyrrolidone) (PVP, molecular weight of ~1.3 × 10^6 g/mol) as viscosity adjustor, which would definitely affect the successive thermal treatment process. In order to determine the proper annealing temperature, thermal properties of dried gel remainder were examined on a TG-DSC system (temperature ranged from 30 to 800 °C). The results (Figure 2) suggest that BFO crystallizes at ~364 °C (the "*" in the figure) and PVP fully volatilizes (or burnt out) at ~520 °C (the arrow in the figure). Using SEM and TEM, we further observed the structure of the samples annealed at different temperatures. With increasing temperature, the fiber diameter was decreased and the fiber surface became rough gradually (see Figure S1 in the Supporting Information). This trend continued until about 450 °C. After that temperature, a quasi-core/shell structure began to form that might be due to the vaporization of PVP. Upon the annealing at 520 °C, the fiber contained almost no residual PVP. The selected area electron diffraction (SAED) patterns shown in Figure 2 also indicate that crystallization started at about ~400 °C and well-defined crystallization patterns began to appear at ~500 °C. Finally, when we employed a 550 °C annealing, the fiber became phase-pure BFO and the diffraction rings in the SAED pattern became bright, sharp and uniform, and the surface of the fiber became rough and dense simultaneously. However, when we further increased the temperature to 600 °C, the grains in the fiber had grown too large, and in this situation, we even cannot acquire continuous diffraction rings from the fiber. The role of another chemical in the solution, 2,4-pentanedione (acetylacetone, or acacH, and $C_5H_8O_2$), is a chelating agent and it helps stabilize the sol system. It is known that acacH is able to bridge (μ-bonding) metal ions although it is not the preferred process in general, and the complex has relatively low thermal decomposition temperatures, giving metal oxide as the primary product.[26,27] Because the mole ratio of acacH over metal ions (Bi^{3+} and Fe^{3+}) is about 2, it can be deduced that all the Bi^{3+} and Fe^{3+} cations are bound to the acacH. So the crystallization process here is actually synchronous with the decomposition process of Bi^{3+}-(acacH)-Fe^{3+} compound under annealed conditions, making it possible to get BFO crystallized at relatively low temperature (as compared with literature data).

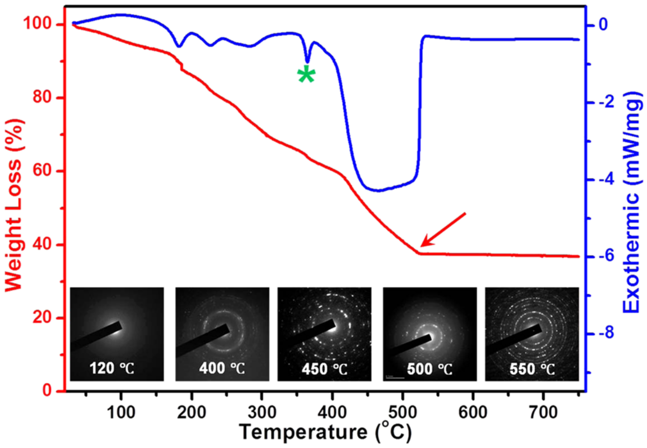

Figure 2. TG-DSC analysis of the crystallization of BFO nanofibers. Insets: the SAED patterns of samples annealed at different temperatures for 2 h.

We further studied the influences of accelerating voltage and PVP concentration on the final product structures and the results are shown in the insets of Figure 1. Changing from 12 to 18 kV, the accelerating voltage was found to have significant influences on the morphology of the nanofibers—the higher the voltage, the smaller the nanofiber diameters. When the voltage is too high (~18 kV for our setup) the nanofibers became less uniform in diameters and some of them would break. We also studied the influence of PVP amount in the precursor solution (presented by X which is defined as the weight ratio of PVP over $Fe(NO_3)_3{\cdot}9H_2O$ in the solution). The inset in Figure 1 presents three typical cases with X = 0.6, 0.75, and 0.9, respectively. When X = 0.6, because of the low viscosity of the solution, we can hardly obtain continuous nanofibers, and consequently, there will be some big droplets generated on the collector because of the disjointed fluid during the electrospinning process. However, when there is excessive PVP (X = 0.9), the nanofibers will shrink seriously after annealing, and they will break into segments easily. So here in this situation, we optimized X = 0.75 to be the most proper parameter.

More detailed structural analysis on BFO sample (annealed at 550 °C) was conducted and the results are shown in Figure 3. Both SEM and TEM observations show clearly the polycrystalline nature of the nanofibers and the grain size is 10−20 nm. The XRD measurements in Figure 3f indicate that BFO has a rhombohedral perovskite structure and no impurity phase was identified. Lattice parameters of BFO nanofibers were calculated using XRD analysis software and the results are as following, $a = b = 0.5569$ nm, $c = 1.387$ nm, $\alpha = \beta = 90°$, and $\gamma = 120°$. All the values of our sample are consistent with the literature data (JCPDS card No. 86−1518), suggesting that our samples are pure perovskite and free of internal stress. The SAED pattern and the corresponding high-resolution TEM (HRTEM) image further confirmed the structural analysis. From the EDS analysis shown in Figure 3e, we can calculate that the atomic ratio of Bi: Fe is almost 1:1. All the analysis from the HRTEM is consistent with the XRD data.

2. Ferroelectric and Piezoelectric Characterizations. Ferroelectric and piezoelectric tests were performed on a scanning probe microscope (SPM) integrated with a module of piezoresponse force microscopy (PFM). In the measurement, the nanofiber is placed on a conductive substrate and a conductive atomic force microscopy (AFM) tip is in contact with the nanofiber, as shown in Figure 4a. Figure 4b shows the topographic image of two nanofibers. From the figure, one may estimate that the nanofiber diameters are around 170 nm, which are consistent with the data obtained from other methods (SEM and TEM). In the piezoelectric measurement, electrical signals from the SPM system were applied on the

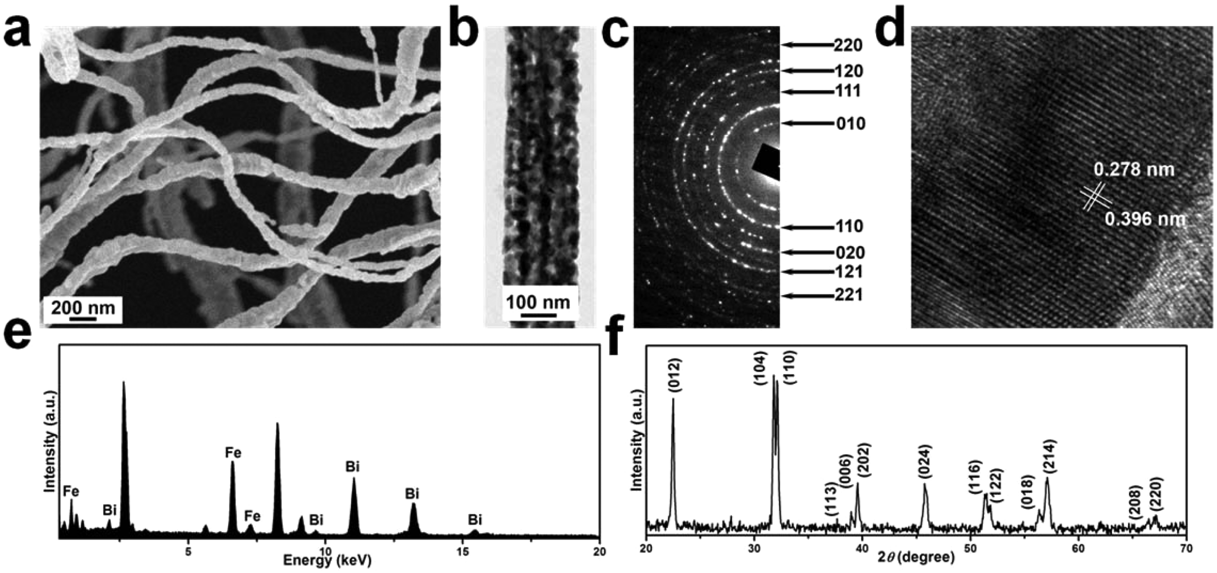

Figure 3. (a) SEM and (b) TEM images of the BFO nanofibers annealed at 550 °C for 2 h; (c−e) corresponding SAED pattern, HRTEM image, and EDS spectra from b) (all unindexed peaks in e are due to the copper grid sample holder used in TEM); and (f) XRD pattern of the annealed nanofibers.

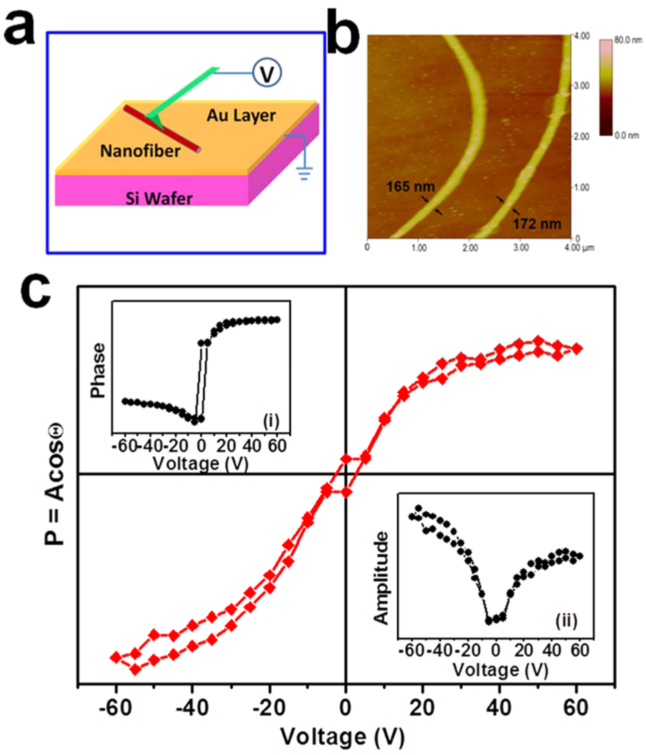

Figure 4. (a) Schematic setup for the PFM measurement; (b) AFM topographic image of nanofibers; and (c) ferroelectric properties of a single nanofiber. Insets (i) and (ii) are the phase-voltage hysteresis loop and the amplitude-voltage butterfly loop, respectively.

nanofibers through the configuration of tip-nanofiber-substrate. The insets of Figure 4c show the signals (phase and amplitude) collected by the microscopy, which are typical piezoelectric responses.[20,29,30] On basis of these data, the polarization of the nanofiber can be calculated using the equation

$$P = A\cos\theta \qquad (1)$$

where P is polarization, A refers to amplitude, and θ refers to phase. With all data put together, a hysteresis loop shown in Figure 4c was obtained. The absolute values of polarization are not available due to the fact that the electrode (i.e., the AFM tip) area cannot be precisely determined. The loop looks very slim due to a couple of factors including the possible poor electrical contact between the AFM tip and the nanofiber as well as the possible large portion of nonswitchable component in the nanofibers.[31] Nevertheless, there is no doubt that the nanofiber has a ferroelectric feature.

3. Ferroelectric Photovoltaic Performance of the Nanofibers. In the literature, two major types of ferroelectric thin film-based photovoltaic devices are reported, as schematically shown in Figure 5a. Devices with a parallel capacitor type of structure (left in Figure 5a) could offer a relatively large photocurrent but low voltage, whereas devices with an in-plane electroded capacitor structure (right in Figure 5a) could generate a relatively high voltage but small photocurrent. The relationship between device performances and material properties for both cases has been well-established. For the structural configuration of our devices (Figure 5b), the calculation of material property is complicated because of the random distribution of the nanofibers. Nevertheless, one may still estimate the values of the parameters with an acceptable precision and accuracy. As the measured current from the photovoltaic device is I (mA), then the average current density J in a single nanofiber is

$$J = \frac{I}{SN} \qquad (2)$$

where S is the average cross-section area of individual nanofiber, and N is the number of nanofibers per unit area (of the substrate). In our sample, the average diameter of the nanofibers is ∼200 nm, so $S = 3.46 \times 10^{-10}$ cm^2. The number of nanofibers on the device, estimated from the SEM image, is ∼7500. If we preset the current of ∼2.5 nA from the $I-V$ curve, the current density can be calculated as $J = ((2.5 \times 10^{-9}$ A$)/(3.46 \times 10^{-10}$ cm$^2 \times 7500)) \approx 1$ mA/cm^2. This value is ∼10 times larger than that of BFO thin films in the literature. From

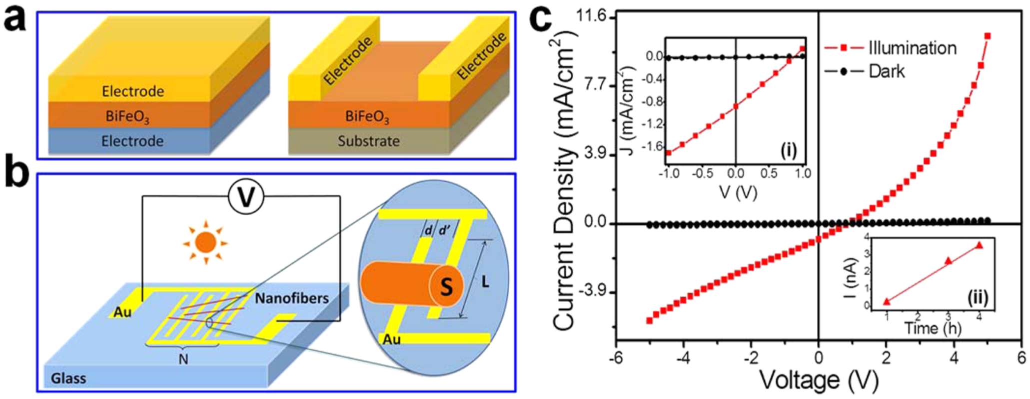

Figure 5. (a) Schematic setup for the measurement of thin film-based photovoltaic devices: left, device with a parallel capacitor configuration; right, device with a laterally aligned interdigital electrodes. (b) Schematic setup for the measurement of random BFO nanofiber-based photovoltaic devices. (c) The photoresponse profile of the nanofibers. Inset (i) shows expanded view of current density behavior around zero-bias. Inset (ii) shows averaged photocurrent after several measurements for different deposition time from 1 to 4 h.

this result we may also estimate the light absorption coefficient of the nanofibers using the equation

$$J(\text{short-circuit current}) = \alpha\beta I_L \tag{3}$$

Where α is the light absorption coefficient, β is the glass linear coefficient (~0.1 cm/V), and I_L is the light intensity (100 mW/cm^2). If we assume J_{SC} to be 1 mA/cm^2, then the value of α is ~1.5×10^7 cm^{-1}. This value is two times of the typical value for BFO thin films in the literature. However, one can further estimate the device current density to be 3.1×10^{-4} mA/cm^2 (see the discussion in the Supporting Information); a value much smaller than the thin film-based photovoltaic devices, which can be further improved by packing more nanofibers on the device from prolonged electrospinning process in the future work.

The reasons for the nanofibers showing enhanced photovoltaic properties could be related to several factors. First, the nanofibers are free-standing (as clearly shown by the XRD and SEM data), whereas the thin films are mechanically clamped by substrates. As generally believed, domain structure and dynamics are critical for the photovoltaic behaviors of the ferroelectric oxides; it is thus understandable that the free-standing feature of the nanofibers makes it possible for the ferroelectric domains switching more freely and efficiently. Second, the nanofibers could trap more photons due to geometric confinement. In the present work, the incident light is along the cross-sectional plane of the nanofibers, which is circular. Multiple reflections or total internal reflections may take place at the material/air interface, which increase the optical path length. Similar idea of "photon trapping" using reflection from a photonic crystal is widely applied in solar cells.[32,33]

■ CONCLUSIONS

In summary, BFO nanofibers have been successfully synthesized via a facile electrospinning process followed by annealing. The influences of processing conditions (annealing temperature, accelerating voltage and PVP concentration) on the nanofiber structure were investigated. Nanofibers prepared under optimized conditions were found to be well-crystallized with a perovskite type of structure and exhibited excellent ferroelectric photovoltaic properties. We have demonstrated that it is possible to make new photovoltaic devices with laterally aligned BFO nanofibers electrically connected with interdigital electrodes.

■ ASSOCIATED CONTENT

Ⓢ Supporting Information

TEM images of nanofibers dried at 120 °C and annealed at different temperatures for 2 h. Discussion on the device current density and efficiency. This material is available free of charge via the Internet at http://pubs.acs.org.

■ AUTHOR INFORMATION

Corresponding Authors

*E-mail: yu.wang@polyu.edu.hk.
*E-mail: yongming.hu09@gmail.com

Author Contributions

⊥L.F. and Y.H. contributed equally. The manuscript was written through contributions of all authors. All authors have given approval to the final version of the manuscript.

Notes

The authors declare no competing financial interest.

■ ACKNOWLEDGMENTS

This work was supported by The Hong Kong Polytechnic University (A-PK29, A-PL53, and G-UC71), the National Science Foundation of China (NSFC 61274073), and National 863 Program (2013AA031903). Support from the Chutian Visiting Scholar Program of Hubei Province of China is also acknowledged.

■ REFERENCES

(1) Fiebig, M.; Lottermoser, T.; Frohlich, D.; Goltsev, A. V.; Pisarev, R. V. Observation of Coupled Magnetic and Electric Domains. *Nature* **2002**, *419*, 818−820.

(2) Eerenstein, W.; Mathur, N. D.; Scott, J. F. Multiferroic and Magnetoelectric Materials. *Nature* **2006**, *442*, 759−765.

(3) Wang, J.; Neaton, J. B.; Zheng, H.; Nagarajan, V.; Ogale, S. B.; Liu, B.; Viehland, D.; Vaithyanathan, V.; Schlom, D. G.; Waghmare, U. V.; Spaldin, N. A.; Rabe, K. M.; Wuttig, M.; Ramesh, R. Epitaxial $BiFeO_3$ Multiferroic Thin Film Heterostructures. *Science* **2003**, *299*, 1719−1722.

(4) Yoshinori, T.; Shinichiro, S. Multiferroics with Spiral Spin Orders. *Adv. Mater.* **2010**, *22*, 1554−1565.

(5) Li, L. J.; Li, J. Y.; Shu, Y. C.; Yen, J. H. The Magnetoelectric Domains and Cross-field Switching in Multiferroic $BiFeO_3$. *Appl. Phys. Lett.* **2008**, *93*, 192506.

(6) Sirenko, A. A.; Bernhard, C.; Golnik, A.; Clark, A. M.; Hao, J. H.; Si, W. D.; Xi, X. X. Soft-mode Hardening in $SrTiO_3$ Thin Films. *Nature* **2000**, *404*, 373−376.

(7) Zheng, R. K.; Wang, Y.; Wang, J.; Wong, K. S.; Chan, H. L. W.; Choy, C. L.; Luo, H. S. Tuning the Electrical Properties of $La_{0.75}Ca_{0.25}MnO_3$ Thin Films by Ferroelectric Polarization, Ferroelectric-field Effect, and Converse Piezoelectric Effect. *Phys. Rev. B* **2006**, *74*, 094427.

(8) Zheng, R. K.; Wang, Y.; Chan, H. L. W.; Choy, C. L.; Luo, H. S. Determination of the Strain Dependence of Resistance in $La_{0.7}Sr_{0.3}MnO_3$/PMN-PT using the Converse Piezoelectric Effect. *Phys. Rev. B* **2007**, *75*, 212102.

(9) Gao, F.; Chen, X. Y.; Yin, K. B.; Dong, S.; Ren, Z. F.; Yuan, F.; Yu, T.; Zou, Z. G.; Liu, J. M. Visible-light Photocatalytic Properties of Weak Magnetic $BiFeO_3$ Nanoparticles. *Adv. Mater.* **2007**, *19*, 2889−2892.

(10) Yu, X. L.; Wang, Y.; Hu, Y. M.; Cao, C. B.; Chan, H. L. W. Gas-sensing Properties of Perovskite $BiFeO_3$ Nanoparticles. *J. Am. Ceram. Soc.* **2009**, *92*, 3105−3107.

(11) Fei, L. F.; Yuan, J. K.; Hu, Y. M.; Wu, C. Z.; Wang, J. L.; Wang, Y. Visible Light Responsive Perovskite $BiFeO_3$ Pills and Rods with Dominant $\{111\}_c$ Facets. *Cryst. Growth Des.* **2011**, *11*, 1049−1053.

(12) Rovillain, P.; de Sousa, R.; Gallais, Y.; Sacuto, A.; Measson, M. A.; Colson, D.; Forget, A.; Bibes, M.; Barthelemy, A.; Cazayous, M. Electric-field Control of Spin Waves at Room Temperature in Multiferroic $BiFeO_3$. *Nat. Mater.* **2010**, *9*, 975−979.

(13) Loh, L.; Briscoe, J.; Dunn, S. Enhanced Performance with Bismuth Ferrite Perovskite in ZnO Nanorod Solid State Solar Cells. *Nanoscale* **2014**, *6*, 7072−7078.

(14) Choi, T.; Lee, S.; Choi, Y. J.; Kiryukhin, V.; Cheong, S. W. Switchable Ferroelectric Diode and Photovoltaic Effect in $BiFeO_3$. *Science* **2009**, *324*, 63−66.

(15) Ji, W.; Yao, K.; Liang, Y. C. Bulk Photovoltaic Effect at Visible Wavelength in Epitaxial Ferroelectric $BiFeO_3$ Thin Films. *Adv. Mater.* **2010**, *22*, 1763−1766.

(16) Seidel, J.; Fu, D. Y.; Yang, S. Y.; Alarcon-Llado, E.; Wu, J. Q.; Ramesh, R.; Ager, J. W. Efficient Photovoltaic Current Generation at Ferroelectric Domain Walls. *Phys. Rev. Lett.* **2011**, *107*, 126805.

(17) Yang, S. Y.; Seidel, J.; Byrnes, S. J.; Shafer, P.; Yang, C. H.; Rossell, M. D.; Yu, P.; Chu, Y. H.; Scott, J. F.; Ager, J. W.; Martin, L. W.; Ramesh, R. Above-bandgap Voltages from Ferroelectric Photovoltaic Devices. *Nat. Nanotechnol* **2010**, *5*, 143−147.

(18) Alexe, M.; Hesse, D. Tip-enhanced Photovoltaic Effects in Bismuth Ferrite. *Nat. Commun.* **2011**, *2*, 256.

(19) Bhatnagar, A.; Chaudhuri, A. R.; Kim, Y. H.; Hesse, D.; Alexe, M. Role of Domain Walls in the Abnormal Photovoltaic Effects in $BiFeO_3$. *Nat. Commun.* **2013**, *4*, 2835.

(20) Wang, Y.; Ganpule, C.; Liu, B. T.; Li, H.; Mori, K.; Hill, B.; Wuttig, M.; Ramesh, R.; Finder, J.; Yu, Z.; Droopad, R.; Eisenbeiser, K. Epitaxial Ferroelectric Pb(Zr, Ti)O_3 Thin Films on Si using $SrTiO_3$ Template Layers. *Appl. Phys. Lett.* **2002**, *80*, 97−99.

(21) Wang, J.; Zheng, H.; Ma, Z.; Prasertchoung, S.; Wuttig, M.; Droopad, R.; Yu, J.; Eisenbeiser, K.; Ramesh, R. Epitaxial $BiFeO_3$ Thin Films on Si. *Appl. Phys. Lett.* **2004**, *85*, 2574−2576.

(22) Zeng, W.; Tao, X. M.; Chen, S.; Shang, S. M.; Chan, H. L. W.; Choy, S. H. Highly Durable All-fiber Nanogenerator for Mechanical Energy Harvesting. *Energy Environ. Sci.* **2013**, *6*, 2631−2638.

(23) Li, D.; Xia, Y. N. Electrospinning of Nanofibers: Reinventing the Wheel? *Adv. Mater.* **2004**, *16*, 1151−1170.

(24) Baji, A.; Mai, Y. W.; Li, Q.; Liu, Y. Electrospinning Induced Ferroelectricity in Poly (vinylidene fluoride) Fibers. *Nanoscale* **2011**, *3*, 3068−3071.

(25) Wang, Y. P.; Zhou, L.; Zhang, M. F.; Chen, X. Y.; Liu, J. M.; Liu, Z. G. Room-temperature Saturated Ferroelectric Polarization in $BiFeO_3$ Ceramics Synthesized by Rapid Liquid Phase Sintering. *Appl. Phys. Lett.* **2004**, *84*, 1731−1733.

(26) Yan, Z.; Wang, K. F.; Qu, J. F.; Wang, Y.; Song, Z. T.; Feng, S. L. Processing and Properties of Yb-doped $BiFeO_3$ Ceramics. *Appl. Phys. Lett.* **2007**, *91*, 082906.

(27) Ghosh, S.; Dasgupta, S.; Sen, A.; Maiti, H. S. Low-temperature Synthesis of Nanosized Bismuth Ferrite by Soft Chemical Route. *J. Am. Ceram. Soc.* **2005**, *88*, 1349−1352.

(28) Han, J. T.; Huang, Y. H.; Wu, X. J.; Wu, C. L.; Wei, W.; Peng, B.; Huang, W.; Goodenough, J. B. Tunable Synthesis of Bismuth Ferrites with Various Morphologies. *Adv. Mater.* **2006**, *18*, 2145−2148.

(29) Hong, S.; Woo, J.; Shin, H.; Jeon, J. U.; Pak, Y. E.; Colla, E. L.; Setter, N.; Kim, E.; No, K. Principle of Ferroelectric Domain Imaging using Atomic Force Microscope. *J. Appl. Phys.* **2001**, *89*, 1377−1386.

(30) Xie, S. H.; Gannepalli, A.; Chen, Q. N.; Liu, Y. M.; Zhou, Y. C.; Proksch, R.; Li, J. Y. High Resolution Quantitative Piezoresponse Force Microscopy of $BiFeO_3$ Nanofibers with Dramatically Enhanced Sensitivity. *Nanoscale* **2012**, *4*, 408−413.

(31) Chen, I. W.; Wang, Y. Activation Field and Fatigue of (Pb,La)(Zr,Ti)O_3 Thin Films. *Appl. Phys. Lett.* **1999**, *75*, 4186−4188.

(32) Yip, C. T.; Huang, H.; Zhou, L.; Xie, K.; Wang, Y.; Feng, T.; Li, J.; Tam, W. Y. Direct and Seamless Coupling of TiO_2 Nanotube Photonic Crystal to Dye-sensitized Solar Cell: a Single-Step Approach. *Adv. Mater.* **2011**, *23*, 5624−5628.

(33) Guo, M.; Xie, K.; Lin, J.; Yong, Z.; Yip, C. T.; Zhou, L.; Wang, Y.; Huang, H. Design and Coupling of Multifunctional TiO_2 Nanotube Photonic Crystal to Nanocrystalline Titania Layer as Semi-transparent Photoanode for Dye-sensitized Solar Cell. *Energy Environ. Sci.* **2012**, *5*, 9881−9888.